

Mixed-Flux Techniques for Rational Synthesis and Structural Control in Silver Chalcogenides

Xiuquan Zhou, Luqing Wang, Hengdi Zhao, Venkata Surya Chaitanya Kolluru, Wenqian Xu, Tieyan Chang, Yu-Sheng Chen, Jianguo Wen, Maria K. Y. Chan, Duck Young Chung, and Mercouri G. Kanatzidis*



Cite This: <https://doi.org/10.1021/jacs.5c04757>



Read Online

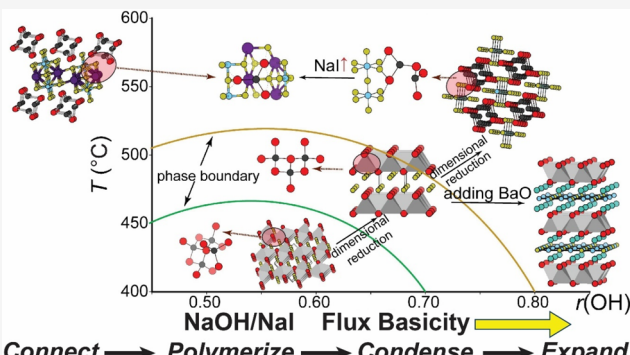
ACCESS |

Metrics & More

Article Recommendations

Supporting Information

ABSTRACT: The functionality of materials is intrinsically linked to their structures, an axiom encapsulated in the principle of structure–property relationships. The pinnacle of materials design is the tailoring of its structure for a specific function, which requires the ability of rational synthesis and the development of synthesis science. This idea, however, remains elusive for the synthesis of complex extended solids. A major obstacle is the difficulty in using established chemical principles selectively to control reaction paths and favor certain structural patterns over numerous other possible results. In this context, we are developing a synthesis science approach that facilitates the control of the structure and bonding to create new structures. This is achieved by employing a two-component flux consisting of mixed hydroxides and halides as the reaction medium. This enables reaction conditions that allow better control of the structure dimensionality and composition by manipulating the temperature and solvent basicity (via the flux component ratio). We demonstrate the efficacy of this method in controlling their structural motifs to arrive at 23 unreported compositions and 6 unique structure types. These materials are expected to exhibit a broad range of properties, from metallic to semiconducting, with calculations suggesting the potential for emergent phenomena such as Dirac semimetals. The reaction paths afforded by these mixed fluxes establish a direct correlation between the synthetic variables and properties, providing significant insight into a broadly applicable approach for new materials.



Downloaded via GEORGETOWN UNIV on May 21, 2025 at 17:55:20 (UTC).
See https://pubs.acs.org/sharingguidelines for options on how to legitimately share published articles.

INTRODUCTION

The vision of “materials by design” is of wide interest because, if implemented at a sufficiently high effectiveness, it could be pivotal in addressing future technological needs. Innovative strategies for designing solid-state materials have been developed by integrating modern synthetic techniques with rational predictions using artificial intelligence, involving structural prediction, symmetry analysis, and the control of critical experimental parameters.^{1–7} Despite considerable progress in predicting properties from materials databases^{8–10} and machine learning,^{11–13} the actualization of predicted structures or compositions remains a challenge due to the limitations of the synthesis science for extended solids compared to molecular compounds. Therefore, to truly realize “materials by design”, the discovery process should transition from a guided “trial-and-error” approach to one driven by rational synthesis methodologies. This requires advancements in synthesis science and understanding of the chemical principles for extended solids.

Our strategy to address this challenge involves the development of new solution-based methods capable of shifting thermodynamic landscapes¹⁴ and leveraging kinetic

control^{15–19} to stabilize metastable compounds and control structural motifs. We seek to uncover and understand new reaction paths that provide rational access to new materials. Our recent work with mixed fluxes (high-temperature solutions) exemplifies this synthetic strategy, allowing us to alter dimensionality and composition by manipulating reaction temperature and flux ratio.^{20–23} In a typical mixed-flux reaction, one component acts as an effective medium, while another countsolvent serves as a tuning knob by varying their ratios. Phase selection is driven by the shifting thermodynamic landscapes of the reaction environment due to the solvent effect of mixed fluxes.²¹ Moreover, it can kinetically stabilize and stack distinct structural motifs to form metastable heterolayered structures.^{20,22} By creating a connection between reaction conditions and structures, our synthetic strategy using

Received: March 19, 2025

Revised: May 12, 2025

Accepted: May 13, 2025

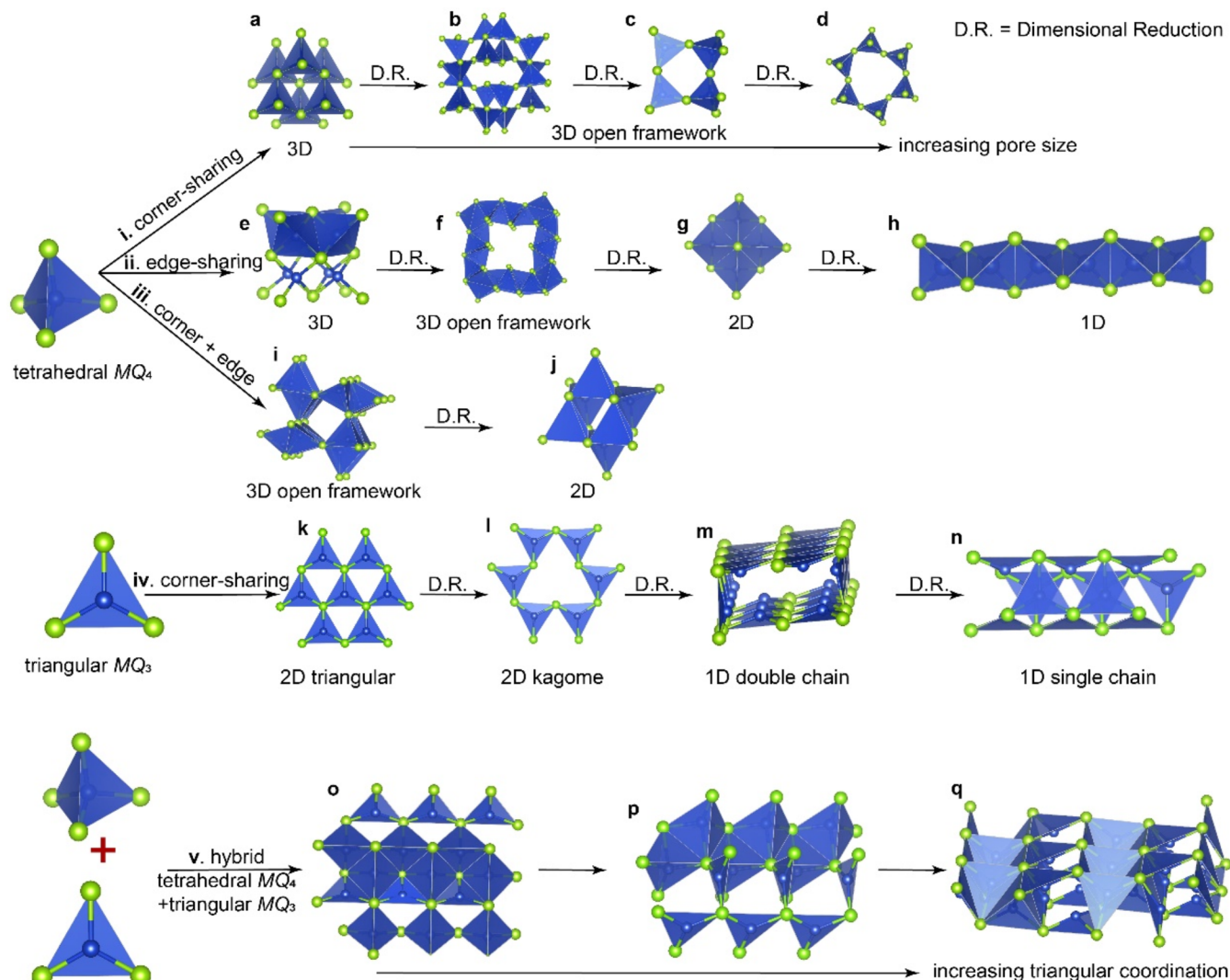


Figure 1. Building complex structures using basic geometric motifs. Structural types built upon corner-sharing tetrahedra: (a) 3D zincblende, (b) open framework with a small cavity, (c) 4-membered, and (d) 6-membered units to accommodate increasing pore size; edge-sharing tetrahedra, (e) antifluorite, (f) hollandite, (g) anti-PbO, and (h), KFeS₂ showing decreasing dimensionality; both corner- and edge-sharing tetrahedra: (i) BaCu₂S₂ and (g) CaAl₂Si₂ types; corner-sharing triangles: (k) 2D triangular lattice, (l) 2D kagome, (m) 1D double chain, and (n) 1D single chain. Hybrid tetrahedral and triangular coordination can lead to even more complex structures shown as (o–q) with increasing fractions of triangular to tetrahedral coordination as 1/3, 1, and 2, respectively.

mixed fluxes can establish a direct correlation between synthetic variables and properties, and can achieve better control and predictability of the resulting structures. For instance, reducing the structural dimension of materials sharing the same elements in their composition can result in an increased band gap.²⁴ This feature can be used to tune semiconductor properties through dimensionality control using mixed fluxes such as the band gap. Furthermore, with fine-tuning of reaction conditions, it is even possible to achieve critical points between metal and semiconductor, leading to emergent properties such as topological semimetals.

The burgeoning field of machine learning (ML) and artificial intelligence (AI) has garnered significant attention for its role in designing and discovering (*in silico*) new materials.^{25,26} These technologies can predict thousands of materials, predominantly new formulas, by substituting elements in known structural types, yet they often fall short in forecasting novel crystal structures. Their predictive power is therefore limited to known structures, leaving truly unpredictable

outcomes beyond their reach. Furthermore, while ML and AI can suggest potential new materials, they typically do not provide synthesis methods, even for compounds that are analogues of known structures.^{27,28} Contrasting this computational approach, work must take place in the laboratory, where we focus on controlling or devising innovative reaction pathways derived from understanding synthetic science. We show that novel unique structures, which AI has difficulty predicting, can be rationally synthesized by controlling basic geometrical components in reaction media. Our approach can facilitate the development of AI to overcome its limitations in predicting entirely new structure types.

In this work, we illustrate the generalizable design scheme of how mixed fluxes can be utilized to stabilize different structural motifs and selectively control their gradual evolution selectively. Building upon our established synthetic methodology, originally developed for copper-based chalcogenides and layered heterostructures^{21,22} we now apply this approach to the distinct chemical landscape of silver-based chalcogenides. This

demonstrates the versatility of our methodology and highlights its broad applicability across varying material systems, underscoring its potential to unlock new structures and compositions across broad classes of materials.

By precisely adjusting reaction conditions within the A(Ba)–Ag–Se (A = alkali metals) system and employing mixed hydroxide/halide fluxes, we not only adapt our approach to new material classes but also uncover unique structures previously unattainable in any system, including those based on copper chalcogenides. This adaptation has enabled us to gain deeper insights into the fundamentals of synthetic science, elucidating how variations in structure and dimensionality can be systematically engineered through rational and tunable synthetic conditions. Moreover, we have discovered a possible link between the evolution of structures and solvated molecular species when reaction conditions are altered. Our research has led to the synthesis of 23 novel structures and compositions, each exhibiting a novel structure, different local bonding, and unique electronic features, such as direct band gaps, Dirac cones, or Weyl points. This advancement in our synthetic approach showcases a refined ability to fine-tune material structures through the rational manipulation of dimensionality and composition, reflecting a significant leap in our understanding of how to discover new materials.

■ RESULTS AND DISCUSSION

Design of Structural Motifs Using Dimensional Reduction. The essence of room temperature coordination chemistry is the ability to design and utilize appropriate ligands dissolved in solutions to coordinate with metal ions under kinetic control. If we view extended solids as vast molecules with infinite coordination networks, then discrete solvated species formed in a high-temperature solution (flux) could exhibit behavior similar to molecular coordination chemistry, thereby influencing product assembly. By stabilizing these molecular species in a high-temperature solution (flux), we could control the metal coordination numbers and structural arrangements, allowing us to manipulate the fundamental building blocks of extended solids. The new rules uncovered through our mixed hydroxide/halide fluxes, particularly the reduction in dimensionality and coordination with higher hydroxide ratios and elevated temperatures, offer useful insights into the structural design using this approach. Direct observation of intermediate building blocks is currently precluded by the challenging reaction environment. Nevertheless, we hypothesize that their solvated forms evolve with reaction conditions, analogous to molecular clusters stabilized differently depending on the solution environment. We propose that these evolving intermediates and their subsequent assembly pathways dictate the final solid-state architectures, thus offering a conceptual framework to understand the observed structure-directing effects within this complex system.

Based on this hypothesis of molecular species and dimensional reduction in mixed fluxes, we can formulate complex structures of extended solids from basic building blocks, such as the examples of MQ_n (M = metal; Q = anion ligand) with tetrahedral ($n = 4$) and triangular ($n = 3$) coordination illustrated in Figure 1. For simplicity, we focus solely on the coordination geometry and disregard the charge balance for MQ_n blocks during this structural design process. For the simplest arrangement of corner-sharing tetrahedra, we have a zinc blend-type structure (Figure 1a). By reducing its dimensionality, we can create three-dimensional (3D) open

framework structures with increasing ring sizes from Figure 1b–1d. This change entails the cornerstone of designing zeolites, which are widely used in catalysis and petroleum industries.^{29,30} Tetrahedra MQ_4 can also form edge-sharing structures such as the antifluorite-type (Figure 1e). With dimensional reduction of the 3D antifluorite, its structure evolves gradually to 3D open framework (hollandite-type,³¹ Figure 1f), 2D (anti-PbO-type,³² Figure 1g) and 1D (KFe_2S_2 -type,³³ Figure 1h). Tetrahedrally coordinated MQ_4 can also be linked via both corner- and edge-sharing to form more distinct structural types, such as the 3D- BaCu_2S_2 -type (Figure 1i) and 2D- CaAl_2Si_2 -type (Figure 1j).

Compared to tetrahedral coordination, structure motifs consisting solely of triangular coordination tend to favor lower dimensionality due to the planar nature of the basic building block. The silver atoms are notorious for adopting variable coordination from tetrahedra to trigonal planar to linear. From a geometrical standpoint, edge-sharing MQ_3 triangles are forbidden as such arrangement leads to shorter M–M bonds than M–Q bonds, which are energetically unfavorable. Thus, the simplest arrangement for this type of coordination is corner-sharing triangles with a triangular lattice formed by M (KZnP-type, Figure 1k), such as in KCuSe .³⁴ From the triangular structure, the dimensionality can be reduced to a 2D kagome lattice (Figure 1l) by incorporation of counterions with higher charges. This insight would be of particular interest to design quantum spin liquid and topological materials with kagome lattice.^{35,36} With further reduction of its dimensionality to 1D, corner-sharing MQ_3 triangles can form homologous chains as shown in Figure 1m,n.

The resulting structures can be even more complex by mixing building blocks of tetrahedral and triangular MQ_n . With increasing ratio (η) of triangular to tetrahedral coordination, the structural motif tends to reduce its dimensionality from 3D open framework ($\eta = 1/3$ in $\text{Ba}_{2-x}\text{Cu}_{5.5}\text{OSe}_4$,²¹ Figure 1o) to 2D ($\eta = 1$ in $\text{K}_3\text{BaCu}_7\text{S}_6$,²¹ Figure 1p). Although the structure remains 2D with higher $\eta = 2$ (CsAg_2S_2 -type,³⁷ Figure 1q), it does show a motif resembling a triangular 1D single chain (Figure 1n), suggesting transforming toward 1D with η approaching infinite.

Now, using mixed AOH/AX (X = halide) fluxes, we illustrate diverse and rationally evolving structural types assembled from simple building blocks using varying coordination numbers and dimensionality. Many diverse structure types can be built by adding design parameters. The coordination number of metal ions and framework dimensionality are selected here as we show that these parameters can be controlled using mixed hydroxide/halide fluxes. We demonstrate that the trend of structural motif evolution illustrated in Figure 1 is generally followed by the A(Ba)–Ag–Se system synthesized using mixed AOH/AX fluxes as the Ag–Se coordination and structural dimensionality reduced with increasing basicity defined as $r(\text{OH}) = n(\text{AOH})/[n(\text{AOH}) + n(\text{AX})]$ and temperature (T) as depicted by the synthetic schemes in Figure 2. We have discovered 23 unreported compounds or compositions including 21 silver chalcogenides and 6 unique structural types (reported in Table 1) using this strategy. In addition, the gradual and predictable evolution of structural motifs allows the fine-tuning of their electronic properties, which provides a direct link between synthetic conditions and properties.

Evolution of Structural Motifs. The synthetic details of reactions and their characterizations are described in the

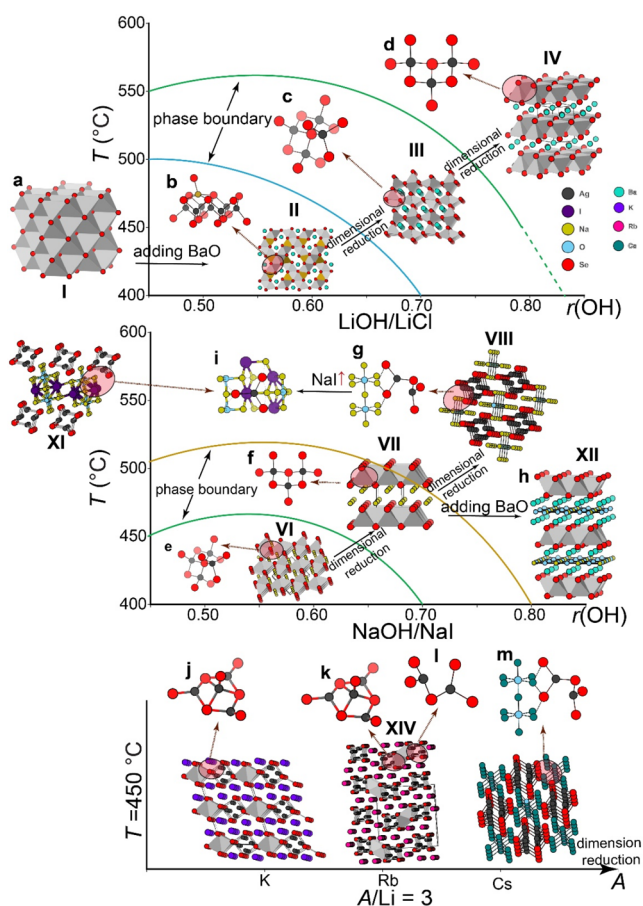


Figure 2. Evolution of structural motifs by successive dimensional reduction. The top and middle panels show the succession of products and corresponding molecular motifs as a function of $r(\text{OH})$ and temperature (T) by using LiOH/LiCl and NaOH/NaI fluxes, respectively. Red atoms are Se. The bottom panel shows reactions using $(\text{Li}, \text{A})\text{OH}/\text{AI}$ for $\text{A} = \text{K}, \text{Rb}$, and Cs at 400°C with $\text{A}/\text{Li} = 3$. (a) Antifluorite in $\text{Li}_{2-x}\text{Ag}_x\text{Se}$ (**I**), the (b) $[\text{Ag}_8\text{Se}_{15}]^{22-}$ fragment in **II** BaAg_4Se_3 , where the brown ball stands for 5-coordinated Ag, (c) $[\text{Ag}_4\text{Se}_{11}]^{18-}$ fragment in an open framework in $\text{BaAg}_{2-x}\text{Li}_x\text{Se}_2$ (**III**), (d) $[\text{Ag}_3\text{Se}_6]^{15-}$ fragment in CaAl_2Si_2 -type BaAg_2Se_2 (**IV**), (e) $[\text{Ag}_4\text{Se}_{11}]^{18-}$ fragment in NaAgSe (**VI**), the same as the (c, f) $[\text{Ag}_3\text{Se}_8]^{13-}$ fragment in anti-PbO-type NaAgSe (**VII**), the same as (d, g) triangular $[\text{AgSe}_3]^{5-}$ fragment interacting with solved $\text{Na}-\text{O}$ in solution that forms the 1D single chain of triangular AgSe_3 in $\text{Na}_{5-x}\text{OAg}_4\text{Se}_4(\text{H}_{1+x})$ (**VIII**), (h) **XI** $(\text{Ba}_{2-x}\text{Na}_x)\text{Na}_{0.3}\text{O}_2\text{Ag}_2\text{Se}_2$, (i) triangular $[\text{AgSe}_3]^{5-}$ fragment interacting with solved $\text{Na}-\text{O}$ and $\text{Na}-\text{I}$ to form **XIII** $\text{Na}_8\text{Ag}_4\text{Se}_4\text{I}_{1.9}\text{O}_2(\text{H}_{1.8})$, (j) $[\text{Ag}_4\text{Se}_7]^{10-}$ fragment in $\text{K}_2\text{Ag}_4\text{Se}_3$, (k) Ag_4Se_7 , and **I**, $[\text{AgSe}_3]^{5-}$ fragment combined to form 1D chains in $\text{Rb}_3\text{Ag}_4\text{Se}_4$ (**XIV**) and (m) solved the $[\text{AgSe}_3]^{5-}$ fragment that forms $\text{Cs}_{4+x}\text{OAg}_4\text{Se}_4(\text{H}_{1+x})$, an analogue to **VIII**. The product for **I** was extremely air-sensitive, and the product was predicted by the reaction trend without being confirmed by single crystal diffraction. Blue, green, and yellow circles show rough phase boundaries among species of (b, c) (or e), (d) (or f), and (g) determined by-products present in our reactions.

Experimental Procedures. Here, we focus on how increasing basicity and temperature can predictably influence the progression of structural motifs in the forming products, enabling controlled manipulation of the reaction paths. For reactions with mixed AOH/AX fluxes, the final product is dictated more by the reaction environment including temperature, basicity, and flux composition than by the initial Q/Ag (or analogous reactant) ratio, as the overall thermodynamic

landscape of the solution and precipitate as a whole controls the reaction pathways. In addition, parameters such as the $r(\text{OH})$ ratio and temperature control the dynamic equilibrium among reactive species, thereby determining the solvated $\text{Ag}-\text{Se}$ fragments that lead to different products. Therefore, as long as Q remains in excess, its starting ratio with Ag is inconsequential as excess Q will remain in the solution as A_2Q . Our observations in related systems consistently indicate that it is the reaction medium that modulates the thermodynamic landscape instead of the reactant ratios that define the resulting structural motifs.

For reactions using LiOH/LiCl , we find that Ag and Li can share the same tetrahedral site in an antifluorite-type structure with compositions of $\text{Li}_{2-x}\text{Ag}_x\text{Se}$ (**I**, Figure 2a and Table S1 and S2 and Figure S1) as illustrated in Figure 2a. This aligns with our geometric analysis of the highest dimension of a 3D structure composed solely of edge-sharing tetrahedra (Figure 1e). From a molecular chemistry perspective, this product could potentially form from the condensation of cubic close-packed (ccp) Se clusters of Ag/Li solvated species present in the flux. It is noteworthy that larger chalcogenide clusters of Ag and Cu compounds often exhibit greater similarity to their respective bulk chalcogenides.³⁸ This is particularly noticeable for some reactions at higher temperatures, where $\text{Ag}-\text{Se}$ building blocks can grow larger, and eventually forming bulk Ag_2Se .^{39,40} Therefore, we propose a possible selenium-ccp fragment of $[\text{Ag}_8\text{Se}_{13}]^{20-}$ (Figure S2) for the formation of **I** based on a known molecular compound of $\text{Ag}_{14}\text{S}(\text{S}-\text{C}_6\text{H}_4-\text{NCS})_{12}(\text{PPh}_3)_8$ exhibiting similar ccp anions. These charged fragments are stabilized by counterions in the highly ionic melt of the flux. Consequently, the reaction medium can significantly influence the stability of the $\text{Ag}-\text{Se}$ fragments under varying conditions, including basicity, ionic composition, and temperature.

When we introduced a countercation Ba^{2+} in the solution by adding BaO to reactions using LiOH/LiCl fluxes, we observed a gradual shift in the structural motifs of the products toward lower dimensionality from **II** BaAg_4Se_3 (Tables S3–S4 and Figure S3a), to **III** $\text{Pnma}-\text{BaAg}_{2-x}\text{Li}_x\text{Se}_2$ (Table S5 and Figure S3b,c) and **IV** $\text{P}3\text{m}-\text{BaAg}_2\text{Se}_2$ (Table S6 and Figure S3d) with increasing $r(\text{OH})$ and T (Figure 2b–d). For low a $r(\text{OH}) = 0.5$ and a low-temperature $T = 450^\circ\text{C}$, the product, **II** BaAg_4Se_3 has a 3D framework isostructural to CaFe_4As_3 ,⁴¹ consisting of edge-sharing AgSe_4 tetrahedra connected by a 5-coordinated square pyramidal AgSe_5 , and its smallest building block can be considered as an $[\text{Ag}_8\text{Se}_{15}]^{22-}$ fragment (Figure 2b). The assembly of the $[\text{Ag}_8\text{Se}_{15}]^{22-}$ block can form BaAg_4Se_3 (**II**) by connecting the square pyramidal AgSe_5 (depicted in brown in Figure 2b) with tetrahedral AgSe_4 (shown in black in Figure 2b) of another cluster as illustrated in Figure S4.

Upon further increasing the hydroxide ratio to $r(\text{OH}) = 0.80$ at 450°C , we observed the gradual emergence of another open framework structure **III** $\text{BaAg}_{2-x}\text{Li}_x\text{Se}_2$ (Figure S3b). This phase features a more expansive framework composed of ribbons of edge-sharing tetrahedral AgSe_4 units, which corner-share to accommodate Ba^{2+} ions (Figure 2c). It can be conceptualized as the condensation of the basic building block of $[\text{Ag}_4\text{Se}_{11}]^{18-}$ (Figure 2c) as illustrated in Figure S5. To completely subvert the BaAg_4Se_3 phase, a $r(\text{OH}) > 0.7$ at 500°C is necessary. By elevating the temperature to 550°C with $r(\text{OH}) = 0.8$, a 2D structure like the CaAl_2Si_2 -type with a composition of BaAg_2Se_2 (**IV**, Figure 2d and Table S6 and

Table 1. Novel Phases Synthesized by Tuning the Flux Ratio and Temperature Using Mixed AOH/AX Fluxes under Selected Synthetic Conditions^a

code	formula	space group	structure type	coordination	dimension	color	flux	<i>r</i> (OH)	T (°C)
I	Li _{2-x} Ag _x Se	<i>Fm</i> ̄ <i>m</i>	antifluorite	Tet	3D	dark red	LiOH/LiCl	0.65	450
II	BaAg _x Se ₄	<i>Pnma</i>	CaFe ₂ As ₄	Sq. Pyr., Tet	3D	black	LiOH/LiCl	0.50	450
III	BaAg _{2-x} Li _x Se ₂	<i>Pnma</i>	BaCu ₂ S ₂	Tet	3D	red	LiOH/LiCl	0.70	500
IV	BaAg _x Se ₂	<i>P</i> ̄ <i>3</i> <i>m</i>	BaAg ₂ S ₂	Tet	2D	red	LiOH/LiCl	0.80	550
V	(Ba _{1-x} Sr _x)Ag ₂ Se ₂	<i>P</i> ̄ <i>3</i> <i>m</i>	BaAg ₂ S ₂	Tet	2D	orange	LiOH/LiCl	0.80	550
VI	NaAgSe	<i>Pnma</i>	TiNiSi	Tet	3D	orange	NaOH/NaI	0.65	450
VII	NaAgSe	<i>P</i> 4/ <i>nmm</i>	PbClF	Tet	2D		NaOH/NaI	0.80	450
VIII	Na _{5-x} OAg ₄ Se ₄ (H _{1+x})	<i>I</i> 4/ <i>m</i>	Nb ₅ Cu ₄ Si ₄	Tr	1D	dark red	NaOH/NaI	0.65	500
IX	K _{5-x} O _{0.5} Ag ₄ Se ₄ (H _x)	<i>I</i> 4/ <i>m</i>	Nb ₅ Cu ₄ Si ₄	Tr	1D	dark red	KOH/NaI	0.80	450
X	Na _{5-x} Pb _x OAg ₄ Se ₄	<i>I</i> 4/ <i>m</i>	Nb ₅ Cu ₄ Si ₄	Tr	1D	black	NaOH/NaI	0.85	500
XI	Na ₈ Ag ₄ Se ₄ I _{1.9} O ₂ H _{1.8}	<i>C</i> 2/ <i>m</i>	unique	Tr	1D/2D	yellow	NaOH/NaI	0.50	600
XII	(Ba _{2-x} Na _x)Na _{0.3} O ₂ Ag ₂ Se ₂	<i>I</i> 4/ <i>mmm</i>	Sr ₂ Mn ₃ Sb ₂ O ₂	Tet	2D	orange	NaOH/NaI	0.80	500
XIII	(Ba _{2-x} K _x)K _{0.3} O ₂ Ag ₂ Se ₂	<i>I</i> 4/ <i>mmm</i>	Sr ₂ Mn ₃ Sb ₂ O ₂	Tet	2D	orange	KOH/KI	0.80	500
XIV	Rb ₃ Ag ₅ Se ₄	<i>Pnma</i>	unique	Tr, Tet	1D	red	(Rb,Li)OH/RbI	0.60	400
XV	CsAg ₃ Te ₂	<i>C</i> 2/ <i>m</i>	CsAg ₃ S ₂	Tr, Tet	2D	black	(Cs,Li)OH/LiCl	0.70	500
XVI	CsBa _{0.8} Ag _{3.4} Se ₃	<i>P</i> 4/ <i>mnm</i>	CsAg ₃ TeS ₂	Tr, Tet	2D	black	(Cs,Li)OH/LiCl	0.70	550
XVII	Ba _{5.3} Rb _{6.7} Ag _{30.7} Se ₂₄	<i>P</i> ̄ <i>1</i>	unique	Tr, Tet	3D	dark red	(Rb,Li)OH/LiCl	0.70	480
XVIII	Ba ₂ Ag _{4-x} Li _x Se ₅	<i>Pnma</i>	BaAg ₂ Se ₅	Tet	2D	red	LiOH/LiCl	0.65	400
XIX	BaAg _{2.5} Se _{2.5}	<i>I</i> 4/ <i>m</i>	hollandite	Tet	3D	black	LiOH/LiCl	0.70	450
XX	Ba ₂ Ag ₄ Se ₂	<i>P</i> 1	unique	Tet	3D	black	LiOH/LiCl	0.55	400
XXI	(K _{0.5} Ba _{1.5})Ag ₂ Se ₄	<i>P</i> 1	unique	Tet	3D	red	(K,Li)OH/LiCl	0.80	400
XXII	SrSe ₂	<i>I</i> 4/ <i>mcm</i>	SrS ₂		2D	orange			400–500
known	BaSe ₃	<i>P</i> 4 ₂ 1 <i>m</i>	BaS ₃		2D	red			400–500
XXIII	BaSeI	<i>P</i> 2 ₁ / <i>c</i>	unique		2D	orange			420

^aThe variable *r*(OH) is defined as $r(\text{OH}) = n(\text{AOH})/[n(\text{AOH}) + n(\text{AX})]$. Symbols Tr, Tet, and Sq. Pyr. represent triangular, tetrahedral, and square pyramidal coordination for Ag–Se bonding, respectively, and 1D, 2D, and 3D represent the structural dimensionality of the product. Crystal structures are provided in the Supporting Data in the form of crystallographic information files (Cifs) available at the Cambridge Crystallographic Data Centre (CCDC) database with deposition numbers: CSD 2387834–2387858.

Figure S3d) is obtained. When the Ba site is substituted with Sr by replacing a portion of BaO with SrO during the reaction, the resulting crystal structure of (Ba_{1-x}Sr_x)Ag₂Se₂ (V) is identical to that of SrAg₂Se₂ (Table S7).²⁰ This suggests a cationic size effect that influences the Ba site but does not affect the arrangement of the Ag–Se blocks. The building block, [Ag₃Se₈]¹³⁻ (Figure 2d), of IV is an even smaller trimer of three edge-sharing tetrahedral AgSe₄. The linking of four corners of two trimers can form a hexamer with 3-fold symmetry, the expansion of which results in the 2D CaAl₂Si₂-type (illustrated in Figure S6a). A similar trimer is also seen in a molecular cluster of [Ag₆(S-C₆H₄-CN)₆(PPh₃)₃] (two trimers in the unit cell), which can condense to form a cluster consisting of the hexamer shown in Figure S6a.⁴²

Our findings suggest that the observed reduction in dimensionality may be associated with the evolution of solvated Ag–Se molecular clusters in the flux, as evidenced by the decrease in the size of basic building blocks from the octamer to tetramer and finally to trimer (Figure 2b–d). To further reduce the structural dimensionality of the product, we conducted reactions using a stronger base of NaOH/NaI as the reaction medium. Interestingly, all reactions below 500 °C resulted in a new ternary phase, V α-NaAgSe (Figure 2e and Table S8 and Figure S7a), which crystallizes in the TiNiSi-type and shares the same Ag–Se 3D open framework motif with III (BaAg_{2-x}Li_xSe₂, Figure 2c). To balance the charge difference between Ba²⁺, there are twice as many Na⁺ ions in the tunnel. Consequently, its basic building block is the same as that of III.

When the reaction temperature increased to 500 °C or higher, the resulting phase was a mixture of Na_{5-x}Ag_xSe₄O-

(H_{1+x}) (VIII, Table S9) and α-NaAgSe (VI), with the fraction of the latter diminishing with higher *r*(OH) and reaction time (Figure S7b). The structure of VIII is isostructural to Na_{5-x}Cu₄Se₄O, consisting of 1D single chains of corner-sharing triangular AgSe₃ (Figures 1n and 2g) separated by Na⁺.²¹ Although we could not refine H positions for VIII using our X-ray diffraction data, we confirmed the presence of a large amount of H for its analogue Na_{5-x}Cu₄Se₄O(H_{1+x}) using neutron diffraction (Figure S4). Therefore, the amount of H in the formula is likely to be 1+*x* to balance the charge.

The basic building unit for VIII is likely a dimer of triangular Ag₂Se₅ (with trigonal planar Ag atoms) connected by a common Se atom (Figure S8) as no discrete [AgSe₃]⁵⁻ monomer was reported, in contrast to [AgQ₄]⁷⁻ tetrahedral monomers.³⁸ However, there is a molecular cluster example that consists of triangular AgQ₃ linked to a tetrahedral AgQ₄ within [Ag₂(SPH)₂(triphos)] (triphos = 1,1,1-tris(diphenylphosphinomethyl)ethane).⁴³ Thus, the basic unit for Ag–Se chains in VIII is likely a dimer such as [Ag₂Se₅]⁸⁻ fragments, which is likely surrounded by solvated Na⁺ in the flux as depicted in Figure 2g. As the basicity or temperature increases, the OH⁻ dissociation toward H₂O and O²⁻ becomes more favorable, resulting in higher O²⁻ concentrations in the flux.⁴⁴ Therefore, as a hard Lewis acid Na⁺ prefers to associate with a hard base O²⁻ or OH⁻ in the flux. This association of Na⁺–O²⁻/OH⁻ is strong, leading to cocrystallization of Na–O chains along with Ag–Se chains as illustrated in Figure S8. The possibility of incorporating solvated species is further evidenced by the formation of XI Na₈Ag₄Se₄I_{1.9}O₂(H_{1.8}) (Figure 2i and Table S10) from a reaction at 600 °C with

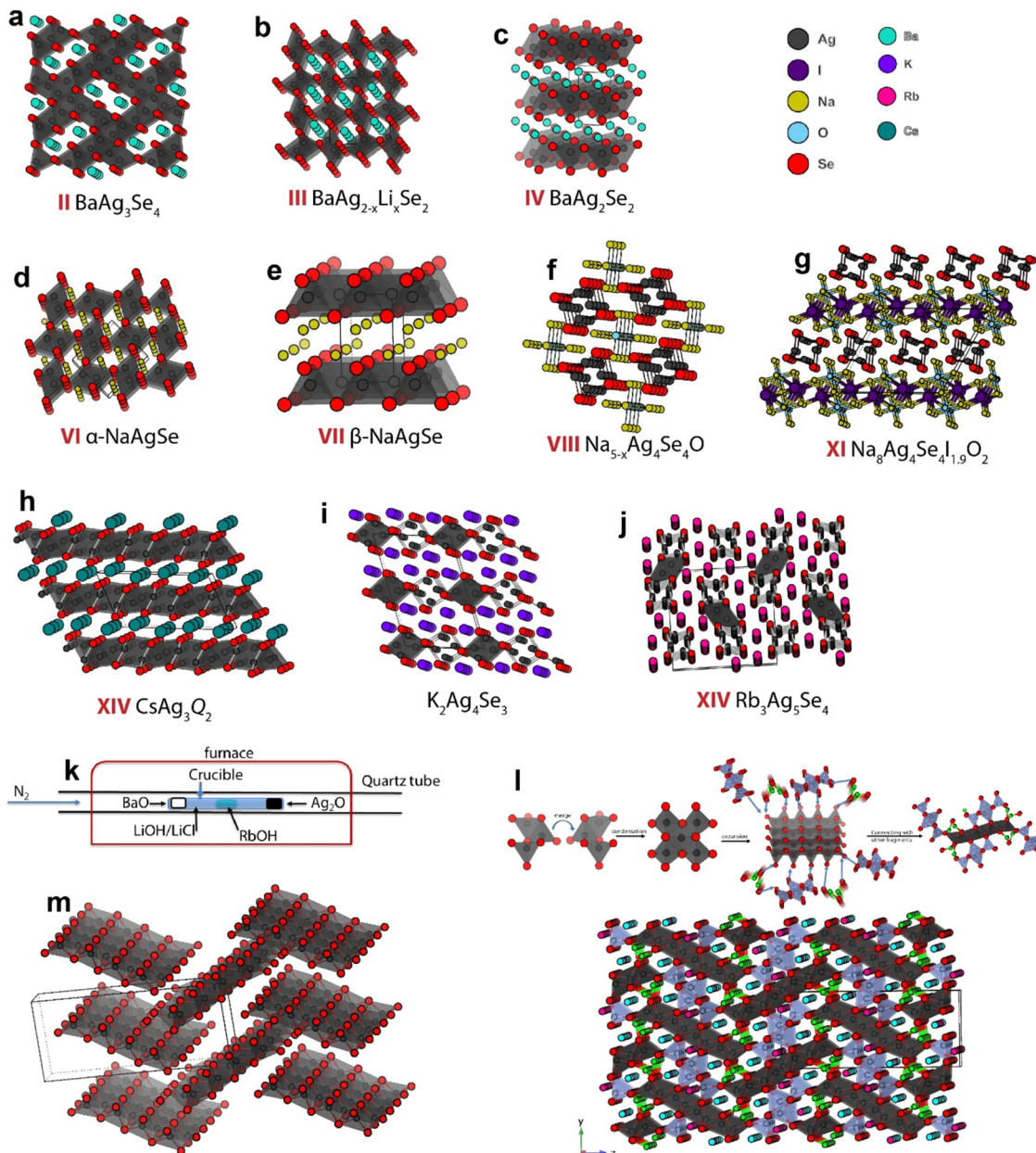


Figure 3. Expanded crystal architectures showcasing broad structural diversity. (a) $\text{II BaAg}_4\text{Se}_3$, (b) $\text{BaAg}_{2-x}\text{Li}_x\text{Se}_2$, (c) BaAg_2Se_2 , (d) $\alpha\text{-NaAgSe}$ (VI), (e) $\beta\text{-NaAgSe}$ (VII), (f) $\text{Na}_{4+x}\text{OAg}_4\text{Se}_4$ (VIII), (g) $\text{Na}_8\text{Ag}_4\text{Se}_4\text{I}_{1.9}\text{O}_2$ (XI), (h) CsAg_3Q_2 (XV), (i) $\text{K}_2\text{Ag}_4\text{Se}_3$, (j) $\text{Rb}_3\text{Ag}_5\text{Se}_4$ (XIV), and (k) a synthetic setup using diffusion method and $\text{Ba}_{5.3}\text{Rb}_{6.7}\text{Ag}_{30.7}\text{Se}_{24}$ (XVII) prepared using the method shown in (l) full and (m) showing only anti-PbO slabs for the framework.

$r(\text{OH}) = 0.5$. Due to the lower solubility of NaI, a mixture of NaOH and NaI with such a ratio can only form a complete melt above 550 °C. This new phase XI consists of AgSe₃ single chains separated by layers of sodium oxyiodide (Figure 2i), suggesting that with the considerable increase of $[\text{I}^-]$ in the flux, the I⁻ ions can partially replace the O²⁻ ions in the solvated Na⁺ species despite their softer Lewis base character.

The abrupt transition in the structural motifs from VI to VIII seemed unusually drastic. To gain a deeper understanding of this change, we conducted panoramic synthesis¹⁹ using *in situ* synchrotron X-ray diffraction to monitor the reaction pathway in real-time, as detailed in the Panoramic Synthesis section in the Appendix. Through panoramic synthesis, we found that $\alpha\text{-NaAgSe}$ (VI) begins to convert to a PbClF-type VII $\beta\text{-NaAgSe}$ (Figures 2f and S10) above 400 °C, consisting

of 2D slabs of edge-sharing AgSe₄ tetrahedra. This structure shares a similar building block as the $[\text{Ag}_3\text{Se}_8]^{13-}$ trimer as IV, despite a different mechanism of formation (Figure S6b). This difference in linking the same building block could be a result of different solvated species of Ba²⁺ in LiOH vs NaOH. This is supported by the evidence that a combination of Ba²⁺ and anti-PbO slabs (tetragonal route in Figure S6b) can be favored with the presence of rocksalt NaO₆ and KO₆ to form heterolayered structures when using NaOH/NaI or KOH/KI fluxes to form $(\text{Ba}_{2-x}\text{Na}_x)\text{Na}_{0.3}\text{O}_2\text{Ag}_2\text{Se}$ (XII, Table S11) and $(\text{Ba}_{2-x}\text{K}_x)\text{K}_{0.3}\text{O}_2\text{Ag}_2\text{Se}$ (XIII, Table S12), respectively.

From the above reaction paths shown in Figure 2a–i, we can establish a series of reaction paths that allow the reduction of 3D structures to 1D with gradual changes of motifs by adjusting the basicity and temperature. This realization is

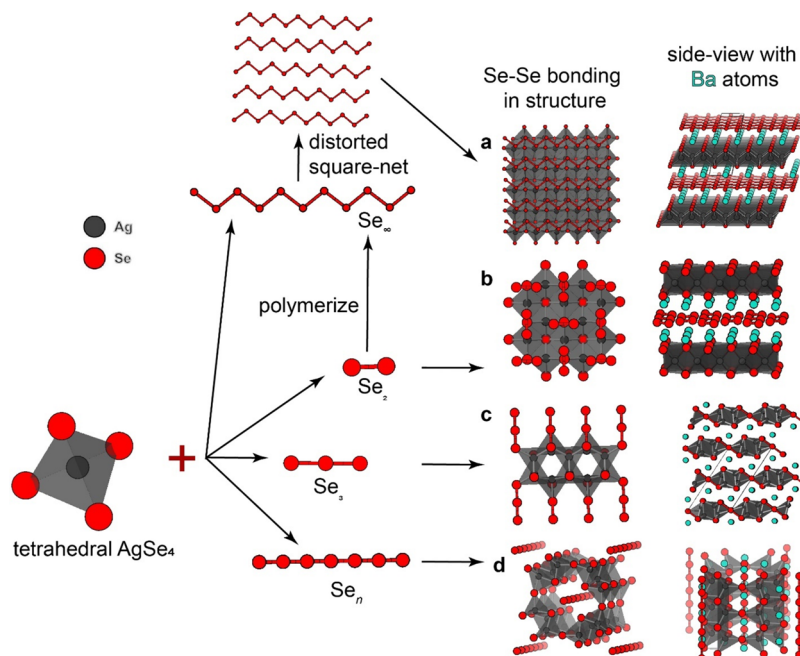


Figure 4. Evolution of structural motifs with the presence of polychalcogenide anions. (a) $\text{Ba}_2\text{Ag}_2\text{Se}_4$ (XX), (b) $\text{Ba}_2\text{Ag}_2\text{Se}_2(\text{Se}_2)$, (c) $\text{Ba}_2\text{Ag}_4\text{Se}_5$ (XVIII), and (d) $\text{BaAg}_{2.5}\text{Se}_{2.5}$ (XIX).

particularly intriguing considering there are no reported ternaries in the Na–Ag–Se system and only two known Ba–Ag–Se ternaries containing polyselenides.^{45,46} We observed that with the increase of basicity by using stronger bases such as NaOH, the Ag^+ ion coordination tended to favor triangular instead of tetrahedral geometries. This is even more so with stronger bases such as KOH, as we obtained $\text{K}_{5-x}\text{Ag}_4\text{Se}_4\text{O}_{0.5}(\text{H}_x)$ (IX, Table S13 and Figure S12), an analogue to VIII, for reaction at 450 °C with $r(\text{OH}) = 0.80$. In comparison, we have stabilized a rare form of AgSe_5 square pyramidal coordination in BaAg_3Se_4 (II) with the lowest basicity and temperature, suggesting a trend of decreasing the Ag^+ coordination number with increasing basicity.

There is difficulty in probing further structural evolution using fluxes of AOH/AI for $\text{A} = \text{K}$, Rb, and Cs as such fluxes tend to reduce Ag^+ to elemental Ag even at moderate temperatures (~500 °C) for relatively low hydroxide ratios (~0.65). This redox effect is complex, and we explain it in detail in SI. Therefore, instead of further probing with higher basicity and temperature, we tested whether we could control the relative ratios (η) between tetrahedral and triangular coordination in the structures by mixing stronger bases with LiOH, which appears to favor tetrahedral AgSe_4 while avoiding the formation of Ag° . When we combined LiOH/LiCl as the primary flux with AOH ($\text{A} = \text{K}$, Rb, and Cs) to achieve $\text{Li}/\text{A} = 5$ and $r(\text{OH}) = 0.70$, reactions involving BaO at 500 °C yielded a mixture of II (BaAg_4Se_3) and III ($\text{BaAg}_{2-x}\text{Li}_x\text{Se}_2$) for $\text{A} = \text{K}$ and Rb. For $\text{A} = \text{Cs}$, the product obtained was CsAg_3Se_2 , which crystallizes in the CsAg_3S_2 -type (Figure S13), consisting of both tetrahedral and triangular AgSe_n ($\eta = 2$).⁴⁷ We carried out a similar reaction, replacing Se with Te, and obtained the new compound CsAg_3Te_2 (XII, Table S14) in this family, suggesting the generalized nature of the reaction paths opened by the mixed fluxes to other systems.

To glean further synthetic insight, we compare and contrast these reactions by also carrying out experiments using AOH/AI ($\text{A} = \text{K}$, Rb, and Cs) as major fluxes mixed with LiOH to

achieve $\text{Li}/\text{A} = 1/3$ and $r(\text{OH}) = 0.70$ at 400 °C. We obtained 2D $\text{K}_2\text{Ag}_4\text{Se}_3$ (Table S14) for $\text{A} = \text{K}$, depicted in Figure 2j.⁴⁸ Its structure features slabs composed of alternating corner-sharing triangular AgSe_3 and edge-sharing AgSe_4 chains (Figure 2j) with $\eta = 3$. Its building block is $[\text{Ag}_4\text{Se}_7]^{10-}$ -fragments, which are composed of both tetrahedral AgSe_4 and triangular AgSe_3 . Such hybrid coordination has been observed in many Ag–Q molecular clusters,³⁸ even a dimer consisting of edge-sharing tetrahedral AgSe_4 and triangular AgSe_3 .⁴³ For $\text{A} = \text{Rb}$ (Figure 2k), η increased to 4 giving the new compound $\text{Rb}_3\text{Ag}_5\text{Se}_4$ (XIV, Table S15). Its structure comprises fragments of the 2D slabs of $\text{K}_2\text{Ag}_4\text{Se}_3$ (Figure 2h) terminated with triangular AgSe_3 chains, thus becoming 1D. This suggests that instead of condensation of $[\text{Ag}_4\text{Se}_7]^{10-}$ tetramers, they are linked with another type of building block, likely $[\text{AgSe}_3]^{5-}$ (Figure 2h). However, for $\text{A} = \text{Cs}$, the product was too air-sensitive to be collected on our diffractometer. Based on the trend, it is likely $\text{Cs}_{4+x}\text{OAg}_4\text{Se}_4$, which is an analogue of VIII. The use of mixed AOH and LiOH fluxes therefore can control the ratio between triangular and tetrahedral coordination by adjusting the solvent's basicity. Furthermore, as we adjust the basicity and introduce more counterions, we can systematically reduce the structural dimensionality.

Building Complex Structures by Motif Control. With our ability to control the structural motifs and coordination of Ag–Se, we aim to demonstrate that this knowledge can be used to kinetically construct unique structure types. To achieve this, we use a kinetically controlled diffusion method to allow different types of building blocks to coprecipitate.²² This level of control is often lacking in solid-state synthesis compared with molecular chemistry because it is challenging to preserve or manage the preferred ligands or basic building blocks during solid-state reactions. To incorporate triangular AgSe_3 , edge- and corner-sharing AgSe_4 units in one structure, we used a 10 cm long glassy-carbon container half-filled with ground LiOH, LiCl, and Se to achieve $r(\text{OH}) = 0.7$ and $r(\text{Se}/\text{OH}) = 0.1$. Then we added Ag_2O to the right end, RbOH (monohydrate)

to the center, and BaO to the left end of the crucible with each area spreading within 1.5 cm. The reaction for this setup (illustrated in Figure 3k) afforded a new black compound $\text{Ba}_{5.3}\text{Rb}_{6.7}\text{Ag}_{30.7}\text{Se}_{24}$ (XVII, Table S16) only at the right end of the crucible. No black crystals of XVII were spotted in the left part or in the center of the crucible. It was also the only phase containing Ag.

The structure of XVII consists of several different types of motifs, including edge-sharing AgSe_4 formed anti-PbO slabs (black tetrahedra in Figure 3l), edge- and BaCu_2S_2 -type corner-sharing tetrahedra chains (blue tetrahedra in Figure 3l), and triangular AgSe_3 chains in the $\text{Nb}_3\text{Cu}_4\text{Si}_4$ -type structure (green triangles in Figure 3l). These motifs can be considered as fragments from Figure 2e,c,f, respectively with an $\eta = 4:1$. The basic framework is built by $8\times\infty$ edge-sharing tetrahedra of isolated anti-PbO slabs (Figure 3m). The corners between each of them are joined by triangular AgSe_3 chains and the BaCu_2S_2 -type motifs filled the space between these sheets. It is noteworthy that the AgSe_3 chains can be broken down to the same Ag_5Se_3 dimer as we suggested for VIII in Figure 2g. Ba and Rb atoms filled the rest of the tunnels enclosed by these different motifs.

Although the structure of XVII is unique and quite complex, its formation is rational. The matrix of the LiOH/LiCl flux favors tetrahedral coordination. At the same time, the RbOH in the center of the reaction vessel promotes the formation of triangular chains, which are predominately located in the central region of the glassy-carbon boat. Additionally, placing BaO at the far-left end of the crucible rather than with Ag_2O (at the right end of the reaction boat) prevents the formation of more stable Ba–Ag–Se compounds that might prematurely precipitate out of the flux. This demonstrates that rationally targeting a specific structural motif is possible using mixed fluxes.

Structural Modification by Anionic Fragments. In addition to incorporating different cationic species, mixed fluxes can stabilize various anions, integrating them into the product when their concentrations in the solution become significant. We first observed a layered compound, $\beta\text{-Ba}_2\text{Ag}_2\text{Se}_4$ (XX, Table S17 and Figure 4a), which appeared around 400 °C and then disappeared above 450 °C during the panoramic synthesis experiment. We initially identified it as $\text{Ba}_2\text{Ag}_2\text{Se}_2(\text{Se}_2)$,⁴⁵ consisting of anti-PbO slabs of $[\text{Ag}_2\text{Se}_2]^{2-}$ (Figure 2e) interleaved by Ba^{2+} and pinwheel $[\text{Se}-\text{Se}]^{2-}$ (Figure 4b), due to their structural similarities and very subtle differences in their PXRD patterns. The difference is that instead of the Se–Se dimer in $\text{Ba}_2\text{Ag}_2\text{Se}_2(\text{Se}_2)$, the Se atoms form polymeric chains or distorted square nets between the $[\text{Ag}_2\text{Se}_2]^{2-}$ sheets (Figure 4a) in XX. By identifying the phase as $\text{Ba}_2\text{Ag}_2\text{Se}_2(\text{Se}_2)$, we hypothesized that an equilibrium between Se^{2-} and Se_2^{2-} could exist at lower temperatures, which is expected to be enhanced by increasing the amount of Se in the flux. These basic fluxes generate polyselenides by the redox disproportionation of elemental Se (e.g., $5\text{Se} + 3[\text{O}]^{2-} \rightarrow \text{SeO}_3^{2-} + 2\text{Se}_2^{2-}$).

As we carried out most reactions with starting molar ratios of Se to hydroxide, $r(\text{Se}/\text{OH}) = n(\text{Se})/n(\text{OH}) = 0.08–0.10$, the equilibrium may shift toward higher polychalcogenides Se_x^{2-} with higher $r(\text{Se}/\text{OH})$. Consequently, we carried out reactions with $r(\text{Se}/\text{OH}) = 0.15$ and $r(\text{OH}) = 0.65$ at 400 °C. This yielded a pure sample of $\text{Ba}_2\text{Ag}_4\text{Se}_5$ (XVIII, Table S18),³⁸ consisting of the structural motifs of BaAg_2Se_2 (IV, Figure 2d) and linear $[\text{Se}-\text{Se}-\text{Se}]^{4-}$ (isoelectronic to I_3^-) as shown in

Figure 4c. It was easily identified as an intermediate phase observed during panoramic synthesis. The reaction also gave BaSe_3 (Table S19) featuring a bent $[\text{Se}-\text{Se}-\text{Se}]^{2-}$ polyselenide configuration instead of the linear $[\text{Se}-\text{Se}-\text{Se}]^{4-}$. This rational approach demonstrates how mixed fluxes can stabilize different anions and incorporate them into the final product once their concentrations in the solution reach a significant level. Further analysis revealed that the Ag site in XVIII could be substituted with Li at higher $r(\text{OH})$ or temperature.

To further understand the formation limits of this intermediate $\text{Ba}_2\text{Ag}_4\text{Se}_5$ phase, we reduced $r(\text{OH})$ from 0.65 to 0.60. We obtained a product with a majority phase of red crystals ($\text{Ba}_2\text{Ag}_4\text{Se}_5$) and dark crystals of $\text{Ba}_2\text{Ag}_2\text{Se}_4$ as a minor fraction (Table S20) with a structure similar to that of $\text{Ba}_2\text{Ag}_2\text{Se}_2(\text{Se}_2)$. However, its Se-net is disordered instead of a dimer, and the layered spacing is 21.658(5) Å at 100 K, slightly larger than that of 21.5784(8) for $\text{Ba}_2\text{Ag}_2\text{Se}_2(\text{Se}_2)$.⁴⁵ We suspected that this could be a kinetic product possessing longer Se–Se chains and carried out a reaction with a higher $r(\text{Se}/\text{OH}) = 0.21$ and a lower $r(\text{OH}) = 0.55$ to preserve these longer fragments. From this reaction, we obtained $\beta\text{-Ba}_2\text{Ag}_2\text{Se}_4$ (XX, Figure 4a and Table S17) crystallizing in the space group of P1 with infinite Se–Se parallel zigzag chains (Figure 4a) inserted between anti-PbO layers of $[\text{Ag}_2\text{Se}_2]^{2-}$. The infinity chain forms a very distorted square net with Se–Se distances within each chain between 2.78 to 3.03 and 3.13–3.32 Å between chains. These are much longer than the typical covalent distance of 2.378(3) Å between Se–Se dimers in $\text{Ba}_2\text{Ag}_2\text{Se}_2(\text{Se}_2)$ or $\alpha\text{-Ba}_2\text{Ag}_2\text{Se}_4$.⁴⁵ In addition, the interlayer distance is 21.892(7) Å at 100 K, 0.3136 Å longer than that for $\text{Ba}_2\text{Ag}_2\text{Se}_2(\text{Se}_2)$, a significant change. This suggests that the crystal with layered spacing between α - and $\beta\text{-Ba}_2\text{Ag}_2\text{Se}_4$ is an intermediate phase consisting of both Se–Se dimers and Se_n polymeric chains. The Ba site in black $\beta\text{-Ba}_2\text{Ag}_2\text{Se}_4$ can be doped with K to form red $\gamma\text{-Ba}_{2-x}\text{K}_x\text{Ag}_2\text{Se}_4$ ($x = 0.55$, XXI, Table S21). K-doping led to the expansion of the layered spacing to 22.488(5) Å about 0.6 Å longer than the undoped phase consistent with a slightly larger ionic radius of K. However, the average bond distances in the Se–Se zigzag chain became shorter between 2.724(18)–2.769(18) Å, whereas the distance between Se atoms in different chains elongates to 3.389(17)–3.342(17) Å. Since the shrinkage of the tetragonal Ag_2Se_2 slabs was negligible after doping K, this change is accommodated in the Se square net, which likely undergoes hole doping.

To see whether such Se zigzag chains could be stabilized without the Ag_2Se_2 layers, we carried out reactions for BaO or SrO without Ag_2O in LiOH/LiCl at 400–500 °C. From unwashed samples, we observed diselenide crystals of binaries BaSe_2 and SrSe_2 (XXII, Table S22) for $r(\text{Se}/\text{OH}) = 0.15$. SrSe_2 was not reported previously and features $[\text{Se}-\text{Se}]^{2-}$ dimers. We also stabilized Se with longer chains in BaSe_3 , K_2Se_4 , and Rb_2Se_5 ; however, no polyselenide Se_n chains with $n > 5$ were observed. These results confirm that there is an equilibrium between selenide and polyselenides, which favors the latter with a higher $r(\text{Se}/\text{OH})$. However, the longer the Se_n chain, the less stable the binary, as binaries with $n > 3$ decomposed almost immediately when in contact with air. Therefore, those with infinite zigzag Se chains were likely stabilized kinetically by the surrounding Ag_2Se_2 slabs.

Since infinite Se chains can be incorporated in 2D layers, it is also possible to stabilize such fragments in 1D structures when

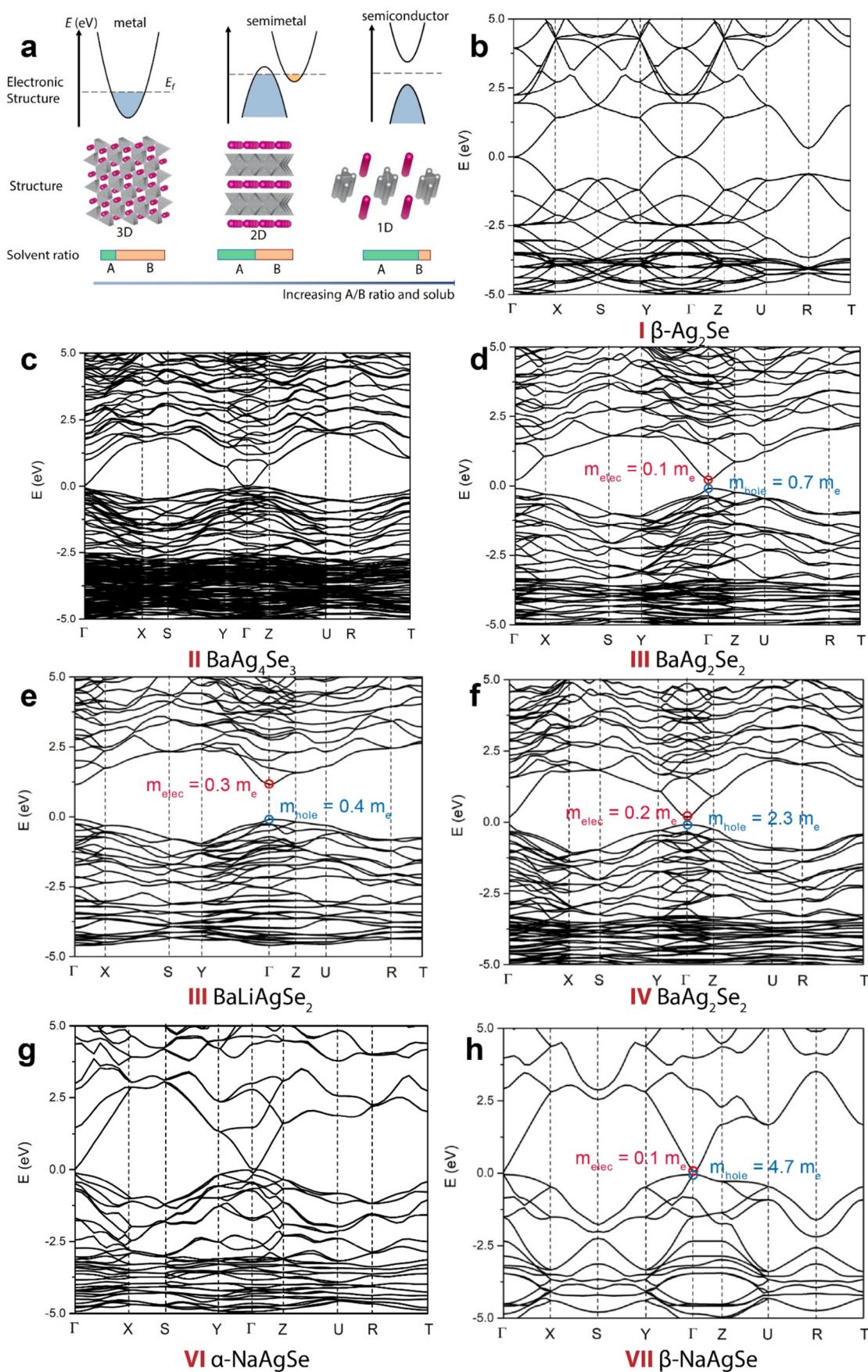


Figure 5. continued

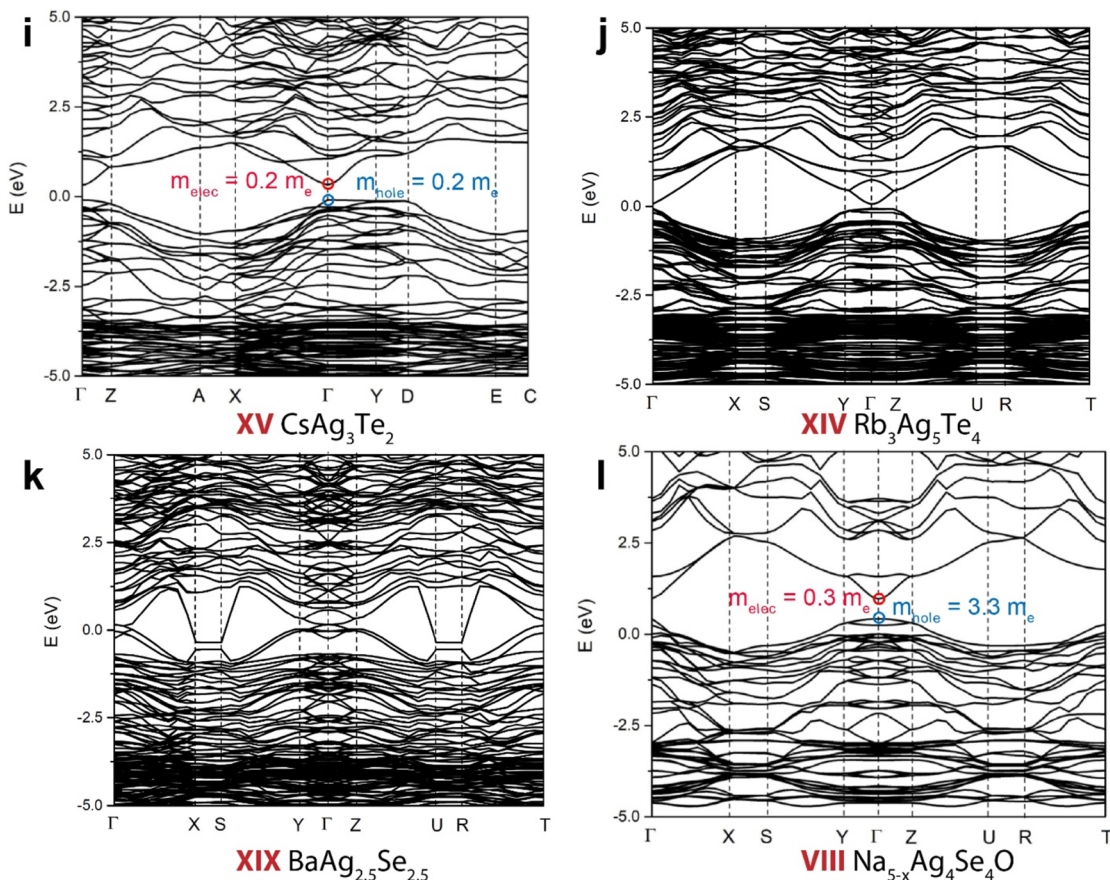


Figure 5. Electronic band structures. (a) Diagram showing correlations between synthetic variables, structures, and electronic structures, and band structures of (b) $\beta\text{-Ag}_2\text{Se}$ (I), (c) BaAg_4Se_3 (II), (d) $Pnma\text{-BaAg}_2\text{Se}_2$ (III), (e) $Pnma\text{-BaLiAgSe}_2$ (III), (f) $\beta\text{-BaAg}_2\text{Se}_2$ (IV), (g) $\alpha\text{-NaAgSe}$ (VI), (h) $\beta\text{-NaAgSe}$ (VII), (i) CsAg_3Te_2 (XV), (j) $\text{Rb}_3\text{Ag}_5\text{Te}_4$ (XIV), (k) $\text{BaAg}_{2.5}\text{Se}_{2.5}$ (XIX), and (l) $\text{Na}_{5-x}\text{OH}_{1+x}\text{Ag}_4\text{Se}_4$ (VIII).

the reaction conditions favor such motifs. For a reaction with $r(\text{Se}/\text{OH}) = 0.2$ and $r(\text{OH}) = 0.70$ at 450°C , we discovered a new compound $\text{BaAg}_{2.5}\text{Se}_{2.5}$ (XIX, Table S23) with longer linear Se chains (disordered chain with $n = 9$ in average instead of infinite) as depicted in Figure 4a. This compound consists of a hollandite-type structure with tunnels enclosed by 4×4 anti-PbO-type Ag–Se ribbons. The tunnels are filled with Ba^{2+} and Se_n chains in the center. We also carried out reactions with $r(\text{Se}/\text{OH}) = 0.15\text{--}0.20$ in NaOH/NaI , but we were unable to recover any polychalcogenide fragments in the product of the Ag–Se systems. These reactions led to the new layered compound of BaSeI or $\text{Ba}_2\text{I}_2(\text{Se}_2)$ (XXIII, Table S24), consisting of both diselenide $[\text{Se}–\text{Se}]^{2-}$ pinwheel layers and I^- layers. This suggests that when a certain flux basicity is exceeded, it does not favor the incorporation polyselenides despite their presence in solution.

Electronic Structures. While synthesis science for rational materials discovery emphasizes controlling reaction pathways, chemical composition, and crystal structures, its ultimate purpose is to achieve the desired chemical and physical properties. These specific properties can be tailored through careful selection of elements in the reactions. The collection of compounds discovered in this work offers a treasure trove of potential physical properties, including those of semiconductors, semimetals, and topological materials. Probing these characteristics, our DFT calculations reveal that the majority of structures identified in this study demonstrate characteristics of either direct band gaps or

semimetal features, as depicted in Figure 5a–l. Although the full analysis of the calculation results is beyond the scope of this report, the salient points in the reported compounds are presented below. Starting from the fluorite-type Ag_2Se (I), it forms a semimetal featuring symmetrical conduction and valence bands at the high symmetry points (Figure 5b). This resembles a nodal line semimetal character but without band crossing.^{49,50} By further reducing the dimensionality, as in BaAg_4Se_3 (II) the band structure features a type II Weyl semimetal as its conduction and valence band cross over at the Γ -point at the Fermi level (Figure 5c).⁵¹ For the 3D $\text{BaAg}_{2.5}\text{Se}_{2.5}$ (XVII) metallic behavior is predicted with large flat bands below the Fermi level (Figure 5k), which are often seen in hollandite-type structures. A gap (Figure 5d) emerges in BaAg_2Se_2 (III), and this gap increases when oAg is substituted with Li (Figure 5e). This substitution also results in a reduced hole effective mass (m_{hole}) from $0.7m_e$ to $0.4m_e$ in BaLiAgSe_2 (III with $x = 0.5$), enhancing mobility. Further dimensional reduction to 2D structures leads to a direct band gap (E_g) of 0.26 eV opening at the Γ -point (Figure 5f) in the 2D BaAg_2Se_2 (IV). For compounds with Na, such as $\alpha\text{-NaAgSe}$ (V) the calculations point to a topological semimetal feature of a quasi-Dirac cone at the Γ -point at the Fermi level (Figure 5g). In comparison, $\beta\text{-NaAgSe}$ is a direct narrow band gap semiconductor with <0.1 eV (Figure 5h). Similarly, $\text{Rb}_3\text{Ag}_5\text{Se}_4$ (XIV) shows a direct band gap of 0.16 eV (Figure 5i). The E_g (direct) value increases to 0.55 eV (Figure 5l) as the $[\text{AgSe}]$ framework converts to the 1D structure of

$\text{Na}_{5-x}\text{OH}_{1+x}\text{Ag}_4\text{Se}_4$ (**VIII**). By creating a bigger oxyhalide block to separate these 1D chains, as in $\text{Na}_8\text{Ag}_4\text{Se}_4\text{I}_{1.9}\text{O}_2(\text{H}_{1.8})$ (**XI**), the E_g (direct) widens to 0.87 eV (Figure S14). This is consistent with our observation of dark red $\text{Na}_{5-x}\text{OH}_{1+x}\text{Ag}_4\text{Se}_4$ (**VIII**) and yellow $\text{Na}_8\text{Ag}_4\text{Se}_4\text{I}_{1.9}\text{O}_2(\text{H}_{1.8})$ (**XI**). The calculations offer early insights into the expected properties, laying the groundwork for future experimentation and in-depth investigations of the optoelectronic properties.

CONCLUSIONS

Our experimental-based general approach advances our knowledge and intuition on how to rationally create new structures and compositions with specific dimensionalities in silver chalcogenides and related materials classes, affording over 23 new materials. Our hypothesized potential connection between dissolved molecular species in hydroxide fluxes and the formation of products with predictable dimensionalities suggests the possibility of a more advanced design approach for building structures from the molecular level. Our results cut across only a small slice of the composition space, and we have succeeded in discovering a large number of unreported structures and compositions. The insights and discoveries into experimental reaction pathways serve to enrich the database of known materials and synthesis methods. The synthesis science and methodology described will also aid advancements in ML and AI within the field of materials science, which generally seeks to leverage existing knowledge to predict materials with known structures. By combining our approach of constructing complex structures from fundamental building blocks with AI, we can overcome its limitations in predicting entirely new structure types. Furthermore, the stability regions of these building blocks could serve as boundary conditions or even training data sets for machine learning models to predict synthetic conditions. Hence, our design strategy has the potential to enable AI to suggest synthetic conditions for the materials that they predict. As the boundaries of what is synthetically possible are expanded, more diverse data sets will be created for computational models.

EXPERIMENTAL PROCEDURES

Synthetic Details. For a typical reaction, Ag_2O and a source of an elemental chalcogen (Q) in the ratio of $\text{Q}/\text{Ag} = 3$ were mixed with a flux of LiOH/LiCl or AOH/AI ($\text{A} = \text{Na}, \text{K}, \text{Rb}, \text{and Cs}$). By varying the ratio between AOH and AX , we have a tuning nob with the nominal hydroxide ratio in the flux, defined as $r(\text{OH}) = \text{mol}(\text{OH})/\text{[mol(OH) + mol(X)]}$. The flux/reactant molar ratios were ~ 5 – 10 to ensure complete initial dissolution. Hence, for each reaction, there were two synthetic parameters: temperature and $r(\text{OH})$. For reactions with stronger bases such as KOH , RbOH , and CsOH , we used Li-modulated fluxes of AOH/AI to reduce the basicity to avoid the reduction of Ag_2O to elemental Ag. In these cases, either LiOH or LiI was added to reach the intended A/Li and hydroxide ratios in the flux. With the hydroxide fluxes, molten AOH allows *in situ* formation of A_2Q by disproportionation of chalcogens (via $6\text{AOH} + 3\text{Q} \rightarrow 2\text{A}_2\text{Q} + \text{A}_2\text{QO}_3 + 3\text{H}_2\text{O}$), obviating a separate synthesis for A_2Q .

The as-purchased NaOH and KOH that we used contained about 10–15% water by weight, and the RbOH and CsOH were monohydrate. Therefore, during the initial heating stage, we observed water leaving the reaction and condensing at the end of the quartz tube, especially above 200 °C. We run our reactions in an open system and under nitrogen flow. This helps to protect the reaction from oxygen and drive the water. In molten hydroxides, such equilibrium exists: $2\text{OH}^- \leftrightarrow \text{H}_2\text{O} + \text{O}^{2-}$, where H_2O and O^{2-} serve as the acid and base, respectively.^{52,53} Under our conditions, water cannot be trapped during the reaction to become a very different type

of flux, known as hydroflux.^{54,55} However, all water can leave the fluxes, since we use an open system under constant N_2 flow. In hydroxide fluxes, the dissociation constant is defined as $K_d = [\text{H}_2\text{O}][\text{O}^{2-}]$.⁴⁴ Since K_d is a function of temperature for a given base, the minimal residual water will always be the same for given conditions. The excess water will be evaporated in such an open system under nitrogen flow, as we observed water condensing at the end of the quartz tube and leaving the reaction when the furnace temperature exceeds 200 °C. Therefore, although the AOH precursors we used contain water, the initial amount of water in the flux is not a determining factor in the observed results.

The reactants were typically in the ratio of $\text{Q}/\text{Cu} = 3$ and the reactant-to-flux ratio is around 0.1–0.2. The total mass of the flux is about 0.8–1.0 g for the 3 mL glassy-carbon boats. The reaction mixture was loaded in a rectangular glassy-carbon boat that was then placed inside a fused silica tube, with each end connected to a metal valve to allow nitrogen gas to flow through. The fused silica tube was placed inside a tube furnace heated to 400–600 °C at a heating rate of 5 °C/min. The temperature was held for 20 h, and then the furnace was either quenched in air or cooled to 300 °C at a rate of 3–6 °C/h followed by turning off the power. The products were washed with water or methanol in an ultrasonication bath to remove the flux. The disproportion of Q led to side products such as A_2QO_x ($x = 3$ or 4), which could be fully dissolved and removed by repeated washing. Although it takes more rounds of washing to remove them with methanol, it is preferred over water if the product is moisture-sensitive.

Panoramic Synthesis. For the collection of *in situ* X-ray diffraction data, we utilized a versatile setup developed at the beamline 17-BM-B at the Advanced Photon Source (APS) with $\lambda = 0.24107 \text{ \AA}$ as described previously.⁵⁶ The reaction vessels can be directly connected to a regular gas cylinder of inert gas (Ar or N_2) in the pressure range between 1 and 3 atm. The vessel can be as large as 3.1 mm, which allows for more materials. In addition, larger capillaries can avoid trapped bubbles when fluxes are molten due to low surface tension compared to smaller ones. The heater is placed beneath the sample, which allows a more uniform temperature. The whole transparent setup allows real-time monitoring of the sample location. Moreover, during reactions, a motor can oscillate the capillary vertically to collect the average information from the entire sample. This robust setup allows rapid screening of *in situ* reactions with simple and fast sample change and alignment.

ASSOCIATED CONTENT

SI Supporting Information

The Supporting Information is available free of charge at <https://pubs.acs.org/doi/10.1021/jacs.5c04757>.

Experimental and computational details, SEM, PXRD, neutron diffraction, single crystal refinement details, and calculated band structure (PDF)

In situ synchrotron powder X-ray diffraction patterns of reactions collected in the mixed-flux of NaOH/NaI for $r(\text{OH}) = 0.65$; crystal structure of $\text{Rb}_3\text{Ag}_5\text{Se}_4$, and crystal structure of $\text{BaAg}_{2.5}\text{Se}_{2.5}$ (PDF)

Accession Codes

Deposition Numbers 2387834–2387858 contain the supporting crystallographic data for this paper. These data can be obtained free of charge via the joint Cambridge Crystallographic Data Centre (CCDC) and Fachinformationszentrum Karlsruhe Access Structures service.

AUTHOR INFORMATION

Corresponding Author

Mercouri G. Kanatzidis – Materials Science Division, Argonne National Laboratory, Lemont, Illinois 60439, United States; Department of Chemistry, Northwestern University,

Evanston, Illinois 60208, United States;  orcid.org/0000-0003-2037-4168; Email: m-kanatzidis@northwestern.edu

Authors

- Xiuquan Zhou** – Materials Science Division, Argonne National Laboratory, Lemont, Illinois 60439, United States; Department of Chemistry, Georgetown University, Washington, District of Columbia 20057, United States
- Luqing Wang** – Center for Nanoscale Materials, Argonne National Laboratory, Lemont, Illinois 60439, United States
- Hengdi Zhao** – Materials Science Division, Argonne National Laboratory, Lemont, Illinois 60439, United States;  orcid.org/0000-0003-4606-6323
- Venkata Surya Chaitanya Kolluru** – Center for Nanoscale Materials, Argonne National Laboratory, Lemont, Illinois 60439, United States;  orcid.org/0000-0003-3057-9749
- Wenqian Xu** – X-ray Science Division, Advanced Photon Source, Argonne National Laboratory, Argonne, Illinois 60439, United States;  orcid.org/0000-0002-4815-6253
- Tieyan Chang** – NSF's ChemMatCARS, Center for Advanced Radiation Sources, The University of Chicago, Argonne, Illinois 60439, United States
- Yu-Sheng Chen** – NSF's ChemMatCARS, Center for Advanced Radiation Sources, The University of Chicago, Argonne, Illinois 60439, United States
- Jianguo Wen** – Center for Nanoscale Materials, Argonne National Laboratory, Lemont, Illinois 60439, United States;  orcid.org/0000-0002-3755-0044
- Maria K. Y. Chan** – Center for Nanoscale Materials, Argonne National Laboratory, Lemont, Illinois 60439, United States;  orcid.org/0000-0003-0922-1363
- Duck Young Chung** – Materials Science Division, Argonne National Laboratory, Lemont, Illinois 60439, United States;  orcid.org/0000-0002-1315-2631

Complete contact information is available at:

<https://pubs.acs.org/10.1021/jacs.Sc04757>

Notes

The authors declare no competing financial interest.

ACKNOWLEDGMENTS

This work was supported by the U.S. Department of Energy, Office of Science, Basic Energy Sciences, Materials Sciences, and the Engineering Division. Work (including SEM, ACAT, and Carbon high performance computing cluster) performed at the Center for Nanoscale Materials, a U.S. Department of Energy Office of Science User Facility, was supported by the U.S. DOE, Office of Basic Energy Sciences, under Contract No. DE-AC02-06CH11357. M.K.Y.C. and V.S.C.K. acknowledge the support from the BES SUFD Early Career award. X.Z. acknowledges support from the Georgetown University startup fund. Work at the beamlines 15-IDD and 17-BM at the Advanced Photon Source (APS) at Argonne National Laboratory was supported by the U.S. Department of Energy, Office of Science, Office of Basic Energy Sciences under Contract No. DE-AC02-06CH11357. NSF's ChemMatCARS Sector 15 is supported by the Divisions of Chemistry (CHE) and Materials Research (DMR), National Science Foundation, under grant number NSF/CHE-1834750 and NSF/CHE-2335833.

REFERENCES

- (1) Nunn, W.; Manjeshwar, A. K.; Yue, J.; Rajapitamahuni, A.; Truttmann, T. K.; Jalan, B. Novel synthesis approach for “stubborn” metals and metal oxides. *Proc. Natl. Acad. Sci. U.S.A.* **2021**, *118*, No. e2105713118.
- (2) Sanchez-Lengeling, B.; Aspuru-Guzik, A. Inverse molecular design using machine learning: Generative models for matter engineering. *Science* **2018**, *361*, 360–365.
- (3) Schmidt, J.; Marques, M. R. G.; Botti, S.; Marques, M. A. L. Recent advances and applications of machine learning in solid-state materials science. *npj Comput. Mater.* **2019**, *5*, No. 83.
- (4) Oganov, A. R.; Pickard, C. J.; Zhu, Q.; Needs, R. J. Structure prediction drives materials discovery. *Nat. Rev. Mater.* **2019**, *4*, 331–348.
- (5) Alberi, K.; Nardelli, M. B.; Zakutayev, A.; Mitas, L.; Curtarolo, S.; Jain, A.; Fornari, M.; Marzari, N.; Takeuchi, I.; Green, M. L. The 2019 materials by design roadmap. *J. Phys. D: Appl. Phys.* **2018**, *52*, No. 013001.
- (6) Tang, F.; Po, H. C.; Vishwanath, A.; Wan, X. Efficient topological materials discovery using symmetry indicators. *Nat. Phys.* **2019**, *15*, 470–476.
- (7) Tabor, D. P.; Roch, L. M.; Saikin, S. K.; Kreisbeck, C.; Sheberla, D.; Montoya, J. H.; Dwarkarnath, S.; Aykol, M.; Ortiz, C.; Tribukait, H.; Amador-Bedolla, C.; Brabec, C. J.; Maruyama, B.; Persson, K. A.; Aspuru-Guzik, A. Accelerating the discovery of materials for clean energy in the era of smart automation. *Nat. Rev. Mater.* **2018**, *3*, 5–20.
- (8) Jain, A.; Ong, S. P.; Hautier, G.; Chen, W.; Richards, W. D.; Dacek, S.; Cholia, S.; Gunter, D.; Skinner, D.; Ceder, G.; Persson, K. A. Commentary: The Materials Project: A materials genome approach to accelerating materials innovation. *APL Mater.* **2013**, *1*, No. 011002.
- (9) Saal, J. E.; Kirklin, S.; Aykol, M.; Meredig, B.; Wolverton, C. Materials Design and Discovery with High-Throughput Density Functional Theory: The Open Quantum Materials Database (OQMD). *JOM* **2013**, *65*, 1501–1509.
- (10) Curtarolo, S.; Morgan, D.; Persson, K.; Rodgers, J.; Ceder, G. Predicting Crystal Structures with Data Mining of Quantum Calculations. *Phys. Rev. Lett.* **2003**, *91*, No. 135503.
- (11) Liu, Y.; Niu, C.; Wang, Z.; Gan, Y.; Zhu, Y.; Sun, S.; Shen, T. Machine learning in materials genome initiative: A review. *J. Mater. Sci. Technol.* **2020**, *57*, 113–122.
- (12) Li, X.; Maffettone, P. M.; Che, Y.; Liu, T.; Chen, L.; Cooper, A. I. Combining machine learning and high-throughput experimentation to discover photocatalytically active organic molecules. *Chem. Sci.* **2021**, *12*, 10742–10754.
- (13) Shen, C.; Li, T.; Zhang, Y.; Xie, R.; Long, T.; Fortunato, N. M.; Liang, F.; Dai, M.; Shen, J.; Wolverton, C. M.; Zhang, H. Accelerated Screening of Ternary Chalcogenides for Potential Photovoltaic Applications. *J. Am. Chem. Soc.* **2023**, *145*, 21925–21936, DOI: [10.1021/jacs.3c06207](https://doi.org/10.1021/jacs.3c06207).
- (14) Jansen, M. A Concept for Synthesis Planning in Solid-State Chemistry. *Angew. Chem., Int. Ed.* **2002**, *41*, 3746–3766.
- (15) Stein, A.; Keller, S. W.; Mallouk, T. E. Turning Down the Heat: Design and Mechanism in Solid-State Synthesis. *Science* **1993**, *259*, 1558–1564.
- (16) Kanatzidis, M. G. Molten alkali-metal polychalcogenides as reagents and solvents for the synthesis of new chalcogenide materials. *Chem. Mater.* **1990**, *2*, 353–363.
- (17) Kanatzidis, M. G. New directions in synthetic solid state chemistry: chalcophosphate salt fluxes for discovery of new multinary solids. *Curr. Opin. Solid State Mater. Sci.* **1997**, *2*, 139–149.
- (18) Kanatzidis, M. G.; Pöttgen, R.; Jeitschko, W. The metal flux: a preparative tool for the exploration of intermetallic compounds. *Angew. Chem., Int. Ed.* **2005**, *44*, 6996–7023.
- (19) Kanatzidis, M. G. Discovery-Synthesis, Design, and Prediction of Chalcogenide Phases. *Inorg. Chem.* **2017**, *56*, 3158–3173.
- (20) Zhou, X.; Wilfong, B.; Chen, X.; Laing, C.; Pandey, I. R.; Chen, Y.-P.; Chen, Y.-S.; Chung, D.-Y.; Kanatzidis, M. G. Sr(Ag_{1-x}Lix)₂Se₂ and [Sr₃Se₂][(Ag_{1-x}Lix)₂Se₂]] Tunable Direct Band

- Gap Semiconductors. *Angew. Chem., Int. Ed.* **2023**, *135*, No. e202301191.
- (21) Zhou, X.; Kolluru, V. S. C.; Xu, W.; Wang, L.; Chang, T.; Chen, Y.-S.; Yu, L.; Wen, J.; Chan, M. K. Y.; Chung, D. Y.; Kanatzidis, M. G. Discovery of chalcogenides structures and compositions using mixed fluxes. *Nature* **2022**, *612*, 72–77.
- (22) Zhou, X.; Malliakas, C. D.; Yakovenko, A. A.; Wilfong, B.; Wang, S. G.; Chen, Y.-S.; Yu, L.; Wen, J.; Balasubramanian, M.; Wang, H.-H.; Chung, D. Y.; Kanatzidis, M. G. Coherent approach to two-dimensional heterolayered oxychalcogenides using molten hydroxides. *Nat. Synth.* **2022**, *1*, 729–737.
- (23) Zhou, X.; Mandia, D. J.; Park, H.; Balasubramanian, M.; Yu, L.; Wen, J.; Yakovenko, A.; Chung, D. Y.; Kanatzidis, M. G. New Compounds and Phase Selection of Nickel Sulfides via Oxidation State Control in Molten Hydroxides. *J. Am. Chem. Soc.* **2021**, *143*, 13646–13654.
- (24) Androulakis, J.; Peter, S. C.; Li, H.; Malliakas, C. D.; Peters, J. A.; Liu, Z.; Wessels, B. W.; Song, J.-H.; Jin, H.; Freeman, A. J.; Kanatzidis, M. G. Dimensional Reduction: A Design Tool for New Radiation Detection Materials. *Adv. Mater.* **2011**, *23*, 4163–4167.
- (25) Merchant, A.; Batzner, S.; Schoenholz, S. S.; Aykol, M.; Cheon, G.; Cubuk, E. D. Scaling deep learning for materials discovery. *Nature* **2023**, *624*, 80–85.
- (26) Szymanski, N. J.; Rendy, B.; Fei, Y.; Kumar, R. E.; He, T.; Milsted, D.; McDermott, M. J.; Gallant, M.; Cubuk, E. D.; Merchant, A.; Kim, H.; Jain, A.; Bartel, C. J.; Persson, K.; Zeng, Y.; Ceder, G. An autonomous laboratory for the accelerated synthesis of novel materials. *Nature* **2023**, *624*, 86–91.
- (27) Leeman, J.; Liu, Y.; Stiles, J.; Lee, S. B.; Bhatt, P.; Schoop, L. M.; Palgrave, R. G. Challenges in High-Throughput Inorganic Materials Prediction and Autonomous Synthesis. *PRX Energy* **2024**, *3*, No. 011002.
- (28) Cheetham, A. K.; Seshadri, R. Artificial Intelligence Driving Materials Discovery? Perspective on the Article: Scaling Deep Learning for Materials Discovery. *Chem. Mater.* **2024**, *36*, 3490–3495.
- (29) Li, J.; Corma, A.; Yu, J. Synthesis of new zeolite structures. *Chem. Soc. Rev.* **2015**, *44*, 7112–7127.
- (30) Ozin, G. A.; Kuperman, A.; Stein, A. Advanced Zeolite, Materials Science. *Angew. Chem., Int. Ed.* **1989**, *28*, 359–376.
- (31) Bystrom, A.; Bystrom, A. M. The crystal structure of hollandite, the related manganese oxide minerals, and [alpha]-MnO₂. *Acta Crystallogr.* **1950**, *3*, 146–154.
- (32) Boher, P.; Garnier, P.; Gavarri, J. R.; Hewat, A. W. Monoxyde quadratique PbO₂(I): Description de la transition structurale ferroélastique. *J. Solid State Chem.* **1985**, *57*, 343–350.
- (33) Bronger, W.; Kyas, A.; Müller, P. The antiferromagnetic structures of KFeS₂, RbFeS₂, KFeSe₂, and RbFeSe₂ and the correlation between magnetic moments and crystal field calculations. *J. Solid State Chem.* **1987**, *70*, 262–270.
- (34) Savelsberg, G. Ternäre Pnictide und Chalkogenide von Alkalimetallen und IB-bzw. IIB-Elementen/On Ternary Pnictides and Chalcogenides of Alkaline Metals and IB-resp. II B-Elements. *Z. Naturforsch., B* **1978**, *33*, 370–373, DOI: 10.1515/znb-1978-0404.
- (35) Guo, H. M.; Franz, M. Topological insulator on the kagome lattice. *Phys. Rev. B* **2009**, *80*, No. 113102.
- (36) Kang, M.; Ye, L.; Fang, S.; You, J.-S.; Levitan, A.; Han, M.; Facio, J. I.; Jozwiak, C.; Bostwick, A.; Rotenberg, E.; Chan, M. K.; McDonald, R. D.; Graf, D.; Kaznatcheev, K.; Vescovo, E.; Bell, D. C.; Kaxiras, E.; van den Brink, J.; Richter, M.; Ghimire, M. P.; Checkelsky, J. G.; Comin, R. Dirac fermions and flat bands in the ideal kagome metal FeSn. *Nat. Mater.* **2020**, *19*, 163–169.
- (37) Burschka, C.; Bronger, W. Über die Struktur von CsAg₃S₂ und RbAg₃S₂. *Z. Anorg. Allg. Chem.* **1977**, *430*, 61–65.
- (38) Fuhr, O.; Dehnen, S.; Fenske, D. Chalcogenide clusters of copper and silver from silylated chalcogenide sources. *Chem. Soc. Rev.* **2013**, *42*, 1871–1906.
- (39) Fenske, D.; Zhu, N.; Langetepe, T. Synthesis and Structure of New Ag–Se Clusters: [Ag₃₀Se₈(SenBu)₁₄(PnPr₃)₈], [Ag₉₀Se₃₈–(SetBu)₁₄(PEt₃)₂₂], [Ag₁₁₄Se₃₄(SenBu)₄₆(PtBu₃)₁₄], [Ag₁₁₂Se₃₂(SenBu)₄₈(PtBu₃)₁₂], and [Ag₁₇₂Se₄₀(SenBu)₉₂–(dppp)₄]. *Angew. Chem., Int. Ed.* **1998**, *37*, 2639–2644.
- (40) Tolman, C. A. Steric effects of phosphorus ligands in organometallic chemistry and homogeneous catalysis. *Chem. Rev.* **1977**, *77*, 313–348.
- (41) Todorov, I.; Chung, D. Y.; Malliakas, C. D.; Li, Q.; Bakas, T.; Douvalis, A.; Trimarchi, G.; Gray, K.; Mitchell, J. F.; Freeman, A. J.; Kanatzidis, M. G. CaFe₄As₃: A Metallic Iron Arsenide with Anisotropic Magnetic and Charge-Transport Properties. *J. Am. Chem. Soc.* **2009**, *131*, S405–S407.
- (42) Langer, R.; Breitung, B.; Wünsche, L.; Fenske, D.; Fuhr, O. *Functionalised Silver Chalcogenide Clusters*; Wiley Online Library, 2011.
- (43) Wang, X.-J.; Langetepe, T.; Fenske, D.; Kang, B.-S. Synthesen und Strukturen der polymeren Silber-Komplexe [Ag₂Cl₂(dppbp)₃]_∞, [Ag₂(SPh)₂(dppe)₃]_∞ und [Ag₂(SPh)₂(triphos)]_∞ sowie der Silber-Chalkogenido-Cluster [Ag₇(SPh)₇(dppm)₃], {[Ag₇(TePh)₇(dppp)₃]₂(dppp)} und [Ag₂₂Cl₁₀(PhCOO)₁₁–(dmf)₃]_∞. *Z. Anorg. Allg. Chem.* **2002**, *628*, 1158–1167.
- (44) Mugavero, S. J., III; Gemmill, W. R.; Roof, I. P.; zur Loye, H.-C. Materials discovery by crystal growth: Lanthanide metal containing oxides of the platinum group metals (Ru, Os, Ir, Rh, Pd, Pt) from molten alkali metal hydroxides. *J. Solid State Chem.* **2009**, *182*, 1950–1963.
- (45) Jana, S.; Ishtiyak, M.; Mesbah, A.; Lebègue, S.; Prakash, J.; Malliakas, C. D.; Ibers, J. A. Synthesis and Characterization of Ba₂Ag₂Se₂ (Se₂). *Inorg. Chem.* **2019**, *58*, 7837–7844.
- (46) Assoud, A.; Xu, J.; Kleinke, H. Structures and physical properties of new semiconducting polyselenides Ba₂Cu_δAg₄–δSe₅ with unprecedented linear Se₃₄-units. *Inorg. Chem.* **2007**, *46*, 9906–9911.
- (47) Rettie, A. J. E.; Ding, J.; Zhou, X.; Johnson, M. J.; Malliakas, C. D.; Osti, N. C.; Chung, D. Y.; Osborn, R.; Delaire, O.; Rosenkranz, S.; Kanatzidis, M. G. A two-dimensional type I superionic conductor. *Nat. Mater.* **2021**, *20*, 1683–1688.
- (48) Bronger, W.; Burschka, C. K₂Ag₄S₃ und Rb₂Ag₄S₃, Synthese und Struktur. *Z. Anorg. Allg. Chem.* **1976**, *425*, 109–116.
- (49) Schoop, L. M.; Ali, M. N.; Straßer, C.; Topp, A.; Varykhakov, A.; Marchenko, D.; Duppel, V.; Parkin, S. S. P.; Lotsch, B. V.; Ast, C. R. Dirac cone protected by non-symmorphic symmetry and three-dimensional Dirac line node in ZrSiS. *Nat. Commun.* **2016**, *7*, No. 11696.
- (50) Shao, Y.; Rudenko, A. N.; Hu, J.; Sun, Z.; Zhu, Y.; Moon, S.; Millis, A. J.; Yuan, S.; Lichtenstein, A. I.; Smirnov, D.; Mao, Z. Q.; Katsnelson, M. I.; Basov, D. N. Electronic correlations in nodal-line semimetals. *Nat. Phys.* **2020**, *16*, 636–641.
- (51) Schoop, L. M.; Pielnhofer, F.; Lotsch, B. V. Chemical Principles of Topological Semimetals. *Chem. Mater.* **2018**, *30*, 3155–3176.
- (52) Flood, H.; Förland, T.; Sillén, L. G.; et al. The acidic and basic properties of oxides. *Acta Chem. Scand.* **1947**, *1*, 592–606.
- (53) Lux, H.; Kuhn, R.; Niedermaier, T. Reaktionen und Gleichgewichte in Alkalihydroxydschmelzen. III. Peroxydgleichgewichte. *Z. Anorg. Allg. Chem.* **1959**, *298*, 285–301.
- (54) Chance, W. M.; Bugaris, D. E.; Sefat, A. S.; zur Loye, H.-C. Crystal growth of new hexahydroxometallates using a hydroflux. *Inorg. Chem.* **2013**, *52*, 11723–11733.
- (55) Bugaris, D. E.; Smith, M. D.; zur Loye, H.-C. Hydroflux crystal growth of platinum group metal hydroxides: Sr₆NaPd₂(OH)₁₇, Li₂Pt(OH)₆, Na₂Pt(OH)₆, Sr₂Pt(OH)₈, and Ba₂Pt(OH)₈. *Inorg. Chem.* **2013**, *52*, 3836–3844.
- (56) Shoemaker, D. P.; Hu, Y.-J.; Chung, D. Y.; Halder, G. J.; Chupas, P. J.; Soderholm, L.; Mitchell, J.; Kanatzidis, M. G. In situ studies of a platform for metastable inorganic crystal growth and materials discovery. *Proc. Natl. Acad. Sci. U.S.A.* **2014**, *111*, 10922–10927.